Shadows of Saturn's Ring Moons in the Dusty E-Ring

Bachelor's thesis in Astronomy

Joni Liljeblad
joni.liljeblad@student.oulu.fi
Space Physics and Astronomy Research Unit
University of Oulu

5.6.2021

Contents

1 Abstract

Moons orbiting within Saturn's diffuse E-Ring cause cylindrical shadows to appear inside the ring at high phase angles when the moons obscure sunlight from areas behind them. These shadows can be observed in multiple images taken on the Cassini-Huygens mission at high phase angles when the ring material is scattering sunlight and dust in the area obstructed by the moon does not scatter sunlight creating a shadow. On this preliminary analysis we focus on the shadows of Enceladus and Tethys and show that this method is viable for inferring local ring properties. Information about the size distribution and light scattering properties of the E-Ring particles can theoretically be inferred from measurements. A preliminary analysis is presented with the goal of investigating whether enough data is present and can meaningful results be produced. A Python program was developed to analyze and extract data from the Cassini-Huygens mission images. This Program is used to analyze shadows in images of the moons Enceladus and Tethys taken with different filters and wavelengths at high phase angles.

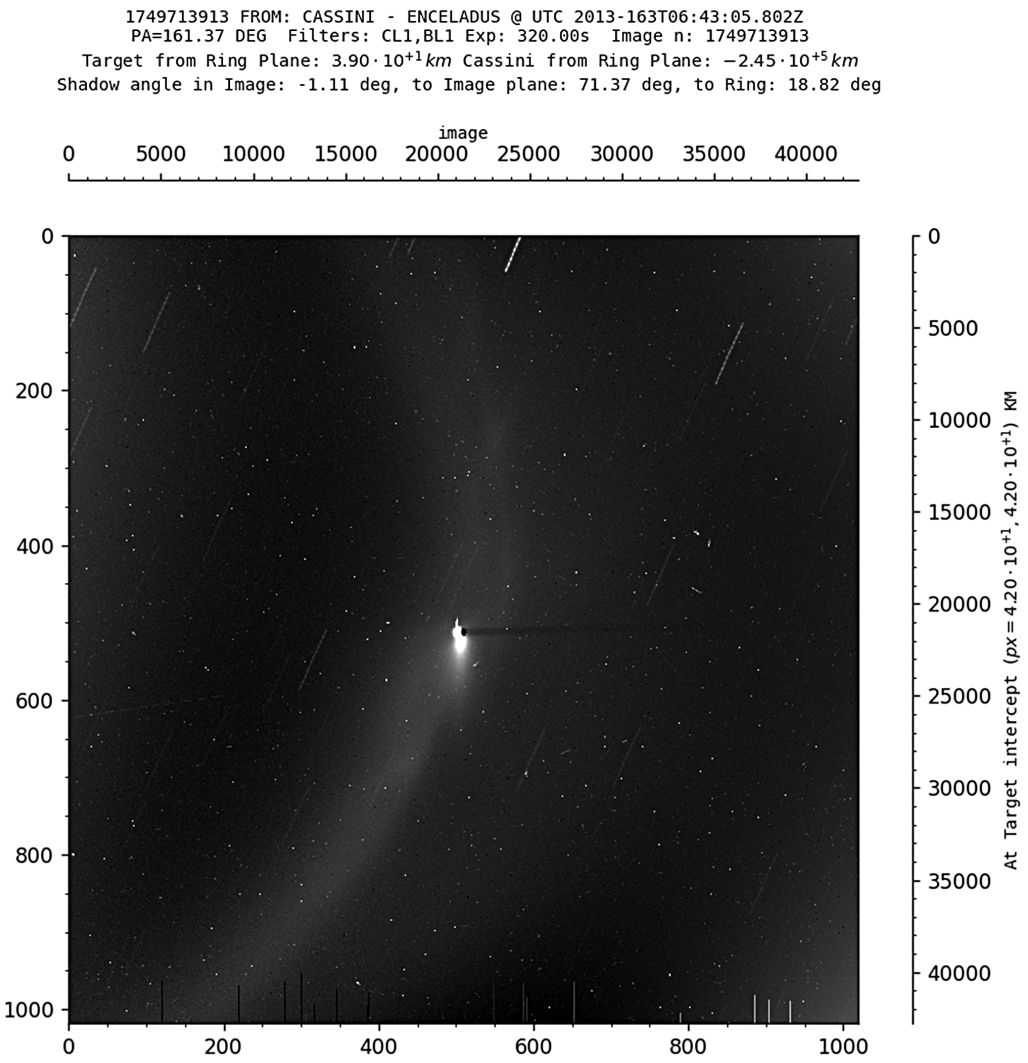

Figure 1: W1749713913 - Image from the Wide Angle Camera on the Cassini Imaging Sub-System giving a clear view of a shadow produced behind Enceladus in the E-Ring when the moon blocks the path of light. The image has added geometry information produced with the help of the NAIF SPICE toolkit (C. H. Acton, 1996).

2 Introduction

The Saturnian system displays the most intricate ring system in the solar system, with dense and thin inner rings which show a variety of very unique features (Cuzzi et al., 2010; Spilker, 2019) and the dusty and diffuse outer rings supplied by the outer moons by various means (Horányi et al., 2009; Kempf et al., 2010; Verbiscer et al., 2009). Especially interesting are the dusty outer rings that are dominated by small micron sized particles, and of these the E-Ring is of special interest because of its unique formation mechanism (Horányi et al., 2009; Ingersoll and Ewald, 2011; Tamayo et al., 2016).

The E-Ring is proposed to mainly consist of water ice particles that are supplied by the moon Enceladus orbiting inside the ring (Kempf et al., 2010; Schmidt et al., 2008). The mechanism is very unique, water jets emerging from the south pole of Enceladus through cracks in its ice shell, ejecting material from inside the moon (Kempf et al., 2010; Porco, 2006; Schmidt et al., 2008). The E-Ring has a very varied brightness profile that peaks around the orbit of Enceladus and shows noticeable differences on different parts of the ring (M. Hedman et al., 2012) and also the particle size distribution varies in different ways in different parts of the ring (M. Hedman et al., 2012; Horányi et al., 2009; Ingersoll and Ewald, 2011; Srama et al., 2011).

Different methods have been used to infer properties of these outer dusty rings from observation with ground based telescopes, remote sensing and in-situ measurements with the Cassini spacecraft (Horányi et al., 2009; Srama et al., 2011; Tamayo et al., 2014; Ye et al., 2016). The largest ring on the outskirts of the Saturnian system, the Peobe ring (Verbiscer et al., 2009), has had its properties and particle size distribution inferred from similar research on the shadows that are formed inside the ring when an object blocks the path of light into a part of the ring in Tamayo et al., 2014 and Tamayo et al., 2016 where using the shadow formed by Saturn on the Pheobe ring some of the local ring properties were inferred, with a similar method used here. An example of a shadow in the E-ring can be seen in Fig. 1 and a overview of the mechanism behind it is detailed in the next section.

In this preliminary analysis similar method to Tamayo et al., 2014 and Tamayo et al., 2016 is discussed and investigated. Firstly the analysis program developed is presented and details and issues related to it are discussed. Afterwards in section 6 the data analysis and results are presented. Lastly the analysis is concluded with a summary of the results and conclusions, including the evaluation of the methods used, and considerations for future research on the topic. The interested reader can skip to section 6.3 for the results.

3 Background and Previous Research

Saturn's E-Ring is special because it is fed by the moon Enceladus, through polar jets ejecting particles from under the moon's icy surface (Kempf et al., 2010; Porco, 2006). There exists a good amount of research on the size properties and distribution of E-Ring particles from measurements of Cassini's different instruments such as the Cosmic Dust Analyzer (Srama et al., 2011, Kempf et al., 2010, Porco, 2006) and Imaging Sub-System (Ingersoll and Ewald, 2011). The Cassini images have been used to infer the total mass for the E-Ring in Ingersoll and Ewald, 2011 and it has been used extensively in the studies of the Enceladus polar jets (Kempf et al., 2010; Porco, 2006; Schmidt et al., 2008).

It has been shown that the E-Ring consists mainly of micron sized particles and that it is replenished by the polar jets on the south pole of Enceladus (Kempf et al., 2010; Srama et al., 2011), and E-Ring properties have been constrained using images before as in Ingersoll and Ewald, 2011 where the images of the E-Ring and the Enceladus plume were used. Also, research on the brightness profile of the E-Ring inferred from images is available (M. Hedman et al., 2012), but the data concerning the shadows in diffuse rings is very limited. There exists research on shadows for the Pheobe ring presented in Tamayo et al., 2014 and Tamayo et al., 2016, but only a single mention of using moon shadows was found in Horányi et al., 2009 p.525. Thus, while not completely novel, the method used is a new look into old data and will hopefully provide another comparison point for previously existing data and help in quantifying the goals and possible research questions for future research.

This preliminary analysis will focus on shadows forming in the dusty E-ring when moons orbiting inside it are viewed from a high phase angle, meaning that the spacecraft is viewing a target from an angle very close to the light/shadow axis, which is the straight line extending outwards from the Sun and going through the target stellar body that is forming the shadow. The shadows are seen because of a brightness difference between the part of the ring that is receiving sunlight and the part that is behind the target. This brightness difference is due to the dusty ring particles scattering received sunlight that can then be observed by a camera on-board the Cassini spacecraft, and due to the obstruction of sunlight a part of the ring directly behind the path of light from the Sun to the target will be observed to have decreased scattering that can be seen as a shadow in images like Fig. 1 and is the same effect as is used in Tamayo et al., 2014 and Tamayo et al., 2016.

4 Motivation

The presence of shadows in the images allows us to potentially gain some information about the local properties of the E-Ring particles. If the data is found to produce meaningful results, it will help in combination with the Cosmic Dust Analyzer measurements from Cassini to constrain the particle size distribution in the E-Ring. Depending on the solar elevation, the shadows will be cast in an angle compared to the E-Ring ring plane and might allow us to probe the particle properties not only in the ring plane, but how they vary in different directions from the ring plane. Any data gained from analyzing the shadows could be used to constrain models of the E-Ring particle distribution and size by comparing the properties of the shadows present in the images to those of which would be produced by the model as was done for the Pheobe ring in Tamayo et al., 2016. At this stage, it is important to investigate data quality and investigate possible difficulties with data acquisition, processing and analysis. Any further analysis would be subject to research project with a much larger scope.

With the results from this preliminary analysis, it can hopefully be concluded whether this approach is viable and is it be able to produce the required data at sufficient precision to be useful for future research. It is important to establish if a large enough dataset can be gathered from the images with a measurable shadow present in them. It is important to confirm the ability to produce data from different wavelengths and from different targets, and to prove the viability of further more in-depth research projects and proposals concerning the topic.

5 Software for the Analysis

5.1 Summary

In short, a program was developed to analyze images taken by the Cassini spacecraft to analyze the shadow contrast produced by the moon orbiting inside the E-Ring at high phase angles. The program is a general utility program and is not restricted to using the Cassini mission data, and could thus be used for analysis on other projects that need a similar toolkit.

The program provides features for viewing VICAR2 image files and performing analysis tasks on them. Currently implemented features include background subtraction, polynomial fitting to brightness profiles and image geometry extraction and viewing.

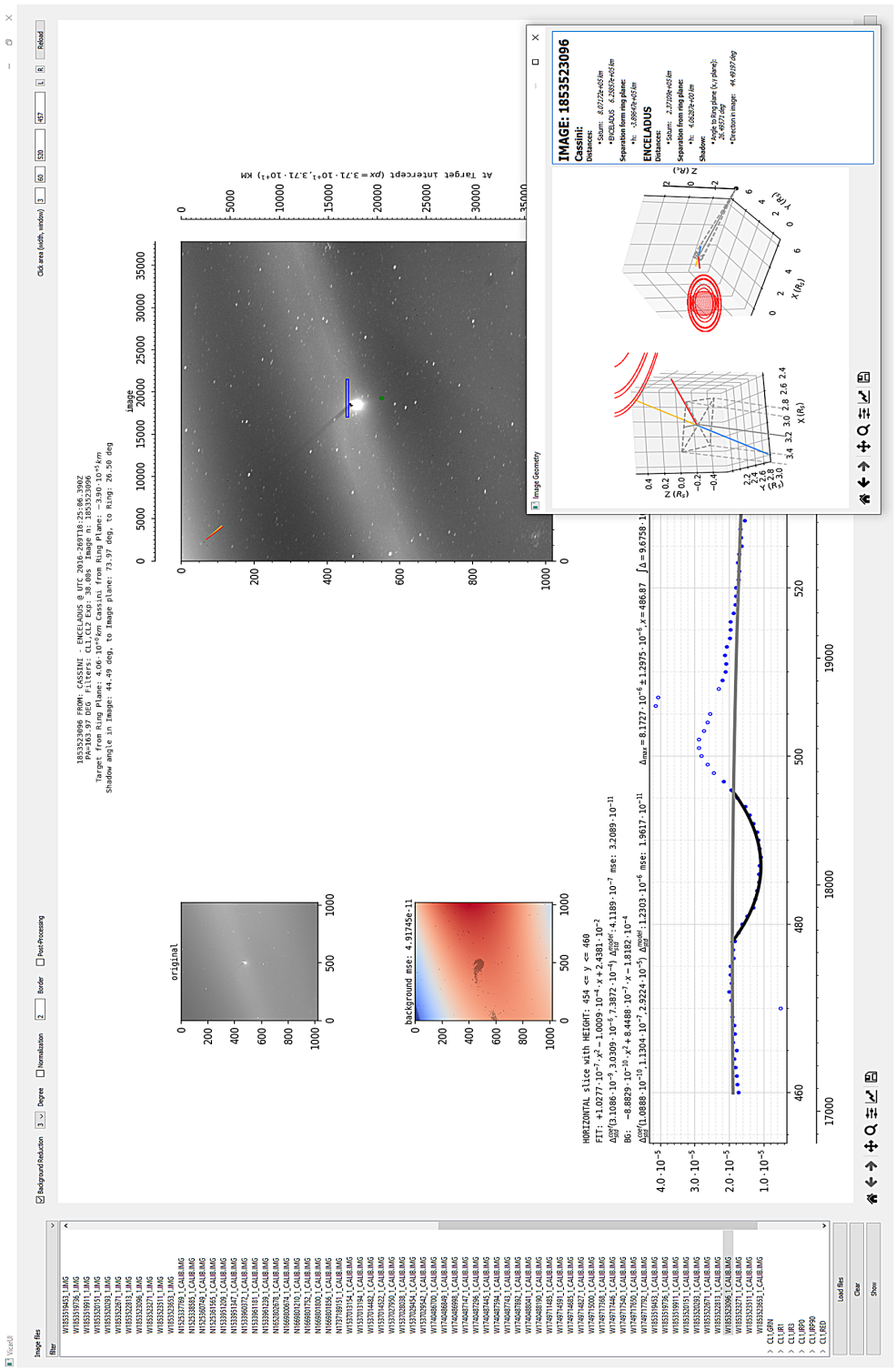

Figure 2: The main UI elements of the program visible. The image shows the basic functionality of background subtraction and polynomial fitting to image samples. The image geometry is displayed in a separate geometry viewer window.

5.2 Details on Implementation

In the following section several models and methods from Scikit (Pedregosa et al., 2011) and Statsmodels (Seabold and Perktold, 2010) are used and short hands for them are defined here:

- OLS (LR) – Linear regression model that performs ordinary least square fits. This model is from Statsmodels and is used with a custom wrapper class to function with Sklearn since there are significant differences between the apis of the two libraries used.
- RANSACRegressor (RR) – An outlier detection algorith for wrapping any linear regression model. This model is used if outlier detection is needed. The model will perform outlier detection as described by the RANSAC-algorithm (Derpanis, 2005). This algorithm is extremely good for data with a lot of outliers, and thus a perfect fit for the background fitting tasks in the program (Choi et al., 2009).
- PolynomialFeatures (PF) – Used to generate polynomial features to the learning sets to make the models fit to higher degree polynomials. No bias included ($include\_bias = False$).
- *mean_ squared_ error* (MSE) - Standard function from SKlearn library that computes the Mean Squared Error between reference data and predicted data.

The program uses pipelines from SKlearn in order to chain different operations together and form workflows for different tasks. The basic composition of a pipeline used in curve fitting applications in the program is described below:

$$input \longrightarrow PF \longrightarrow LR\,or\,RR \longrightarrow output. \tag{1}$$

The necessity to readily obtain reliable metrics about function fits done by the program led to the choice of using Statsmodels as the base model classes. Statsmodels provides parameter standard error and many other metrics without requiring custom solutions to get these metrics. It could be argued that a similar accuracy could be reached by using *curve_fit* from the Scipy (Virtanen et al., 2020) library, but it would mean implementing custom fitting procedures for each task instead of using pipelines and ready made models.

5.2.1 Image Area Inspector

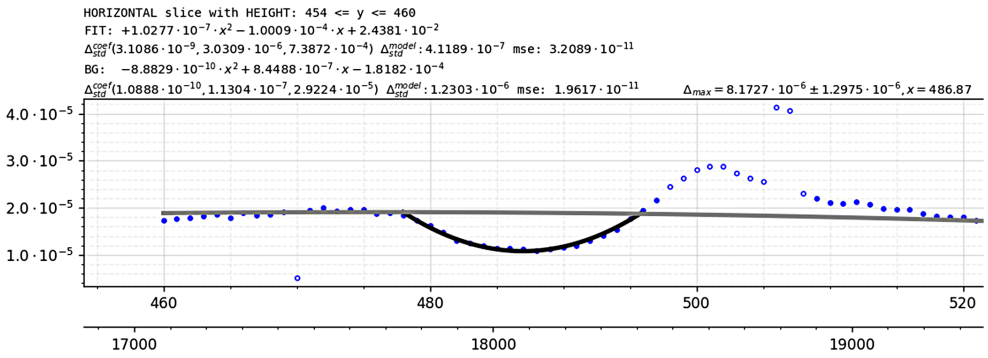

Figure 3: Closeup of the image inspector after a polynomial fit has been performed. The details about fits are presented above the inspection view and the modeled polynomials are plotted in the view. In the plot two polynomial fits can be seen, the gray line - Background Fit, and the black line - Shadow Fit. Opaque dots represent pixel values and rings represents pixels detected as outliers by the background fit. The same view is also visible in Fig. 2 where the outlier feature of the right edge can be identified as an area corresponding to overexposed pixels.

The image area inspector allows the inspection of a user configurable slice of the image in either vertical or horizontal direction with configurable parameters.

- Width – The width of the inspection window from which data will be averaged $(1 + 2 \cdot width)$
- Window – The inspection window size, sets the x-axis of the image area inspector $(1 + 2 \cdot window)$

The program will perform a 2nd degree polynomial fit to the displayed data in the inspector view, displayed in Fig. 3, when the user gives the program a start and an end point. These fits represent the Shadow Fit and Background Fit. Both fits will be displayed with equations reconstructed from the models and the model error. In addition, background model outliers are displayed on the produced plot. The models used are a LR model for the shadow fit and a RR wrapped LR in which the RR model finds the most suitable LR model by removing outliers from the background. The outlier detection can be seen

in Fig. 3 where a part of the pixels in the image inspection area are marked as outliers by the fitting routine and are thus excluded from final polynomial fit, clearly highlighting the effectiveness of the RANSAC algorithm.

Shadow contrast calculation has its own error metric defined based on the standard errors of fit parameters. Shadow contrast error is defined as the square root of the sum of standard errors of background and foreground models. The integral and contrast are estimated by taking x as absolute truth and assuming no error in it. The error for contrast is taken from the standard error calculation of the sum of two variables

$$\Delta_{contrast} = \sqrt{\Delta_{std}^{bg^2} + \Delta_{std}^{fg^2}} \tag{2}$$

where Δ parameters express the standard error of estimate for the background and foreground fits. Integral error is modeled as having this same error for each point on the integration interval and is evaluated as such with the equation

$$\Delta_{Integral} = (b - a) \cdot \sqrt{\Delta_{std}^{bg^2} + \Delta_{std}^{fg^2}} \tag{3}$$

where b and a are the integration limits and Δ parameters are the standard errors for models. These metrics give a useful estimate of the total error.

5.2.2 Autofit

Additional analysis utilities were developed to analyze the shadow contrast further in Cassini images. The developed routine called Autofit collects shadow contrast data based on initial user input and extracted geometry information from SPICE kernels. Collected data is presented as plots and polynomial fitting is performed. This tool was used to perform the majority of data analysis for this paper. An example is provided in Figure 9.

It should be noted that the error propagation from the contrast and integral measurements is not modeled in the *Autofit* functions in the general case, instead a regular ordinary least squares fit is performed with the help of RANSAC doing outlier detection, but a single error accounting power law model is implemented.

5.2.3 Background Subtraction

Background reduction is performed using the pipeline described earlier (1) with RR model wrapping a LR base model. Input features are pixel x,y-coordinates and additional features are generated by PF based on user input. The trained model is used to produce a background model for the

image, model outliers, and a background map, along with the *MSE*-error from comparing the image data with the model predicted background. A possible improvement of the model would be to employ a different fitting scheme or employ an image de-convolution algorithm to to produce a background where the image brightness doesn't get reduced below zero producing artifacts (Puetter et al., 2005).

A similar approach is described shortly in the supplementary information of Schmidt et al., 2008 where a polynomial background subtraction is performed by excluding a region of the image around Enceladus completely. The approach used here is different from the one in Schmidt et al., 2008 as it does outlier detection automatically and is thus able to perform reduction without user intervention. The drawback for this approach is that the performance degrades as we move to foreground dominated data and increased computational cost (Choi et al., 2009). The approach introduced here work well on the WAC (Wide Angle Camera) images, but does not perform well on NAC (Narrow Angle Camera) images of he Cassini ISS (Imaging Sub-System), because the NAC images usually have the target covering a significant portion of the image. The effect of large foreground objects in a blind fit is shown in Fig. 4 where background subtraction is attempted on a NAC image with a large part of the image consisting entirely of a foreground object, Enceladus, leading to failed subtraction procedure where the routine identifies around 90% of the whole image as outliers and fits a background based on a very narrow slice of the image not representative of the actual background. This result differs fundamentally from Fig. 5 where the routine was able to produce a background that corresponds to the original image well and identifying correct areas as outliers.

More work is needed on denoising images or alternatively stacking the images to produce a higher signal-to-noise ratio result. There are successful examples of image stacking and denoising used on Earth based telescope systems (Gwyn, 2008) which could perhaps be adapted to use in Cassini images. A comprehensive overview on image reconstruction, including denoising and background subtraction is presented in Puetter et al., 2005 and is certainly useful on further research on the topic. If the current machine learning approach is continued and is expanded upon Graff et al., 2014 offers in-depth discussion on the topic and introduces a neural network training tool specifically created for astronomy. For further analysis of low signal contrast data the methods used in Tamayo et al., 2014 and Tamayo et al., 2016 could be employed.

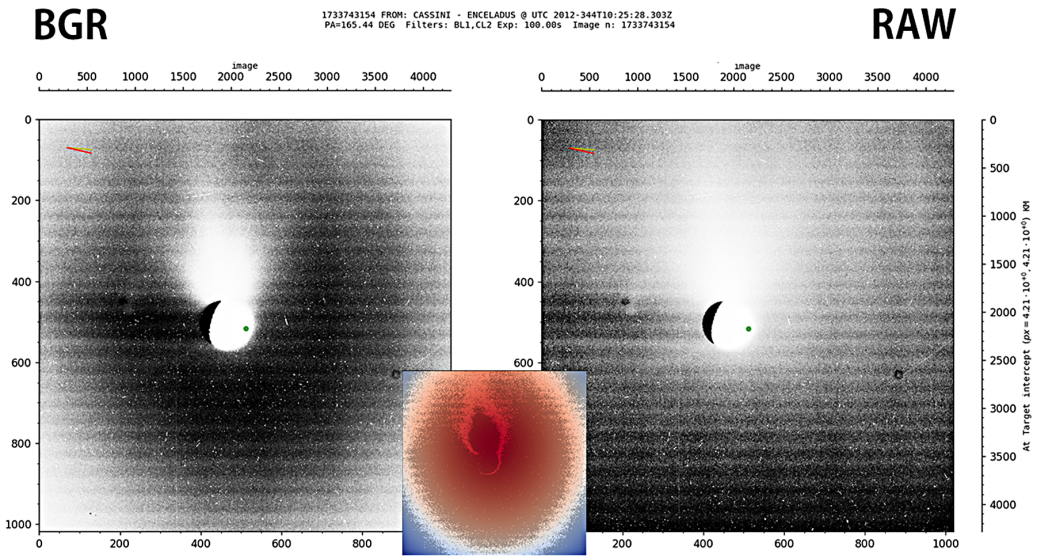

Figure 4: Comparison of background subtracted image and original with Histogram Equalization stretch showing the artifacts produced by background reduction on a NAC image. In the middle the program generated background model is seen and it is clear that the method does not perform well these type of images as almost the whole image is labeled as an outlier (black) in the background fit view in the middle. The parts actually used for the background fit is the white ring showing in the background fit window in the middle, corresponding to the edge of the white gradient in the subtracted image. Even from the amount of outliers the model has detected (90% of the image) it is clear that the routine has failed. The background subtracted image is not usable for analysis as the reduction is not reliable, showing a large contrast to the method used in Schmidt et al., 2008. In addition, the stretched image shows a visible shadow, but also a very large noise threshold, a prime candidate for denoising and stacking. The banding is caused by the "2-Hz" noise, reduced by image calibration (Knowles et al., 2020). The background was modeled as a 2nd degree polynomial. Do note that due to the image stretching applied the pixels corresponding to the target body are severely saturated and does not represent the true lighting conditions of the image in any way. In the original image the sunlight can be observed as a small patch of illuminated edge at the very right edge of the target corresponding to a 164.44 degree phase angle and the shadow is significantly foreshortened, protruding from the image towards the viewer if it were visualized in 3d.

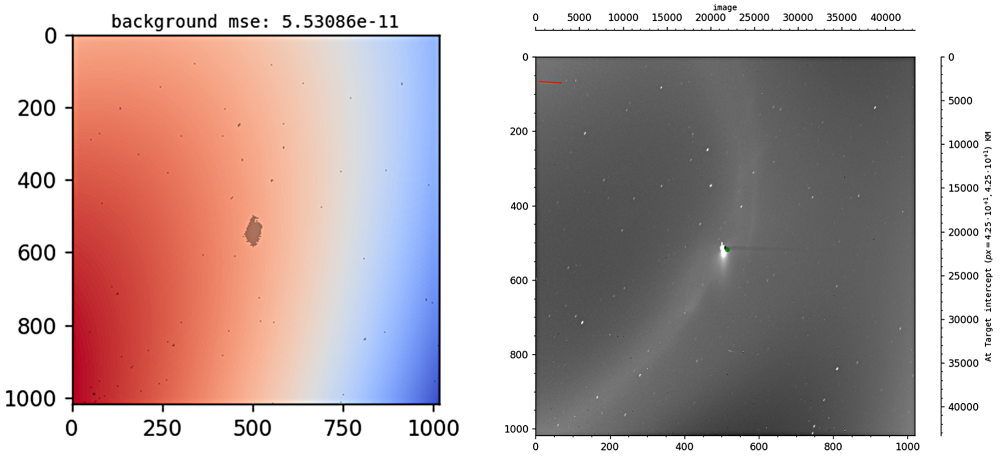

Figure 5: Display of a generated background and the reference image. The background model shows a black patch in the middle corresponding to over-exposed pixels in the original image. In this case, the model successfully identified Enceladus and its plume from the original image as outliers. The background produced a well fitting model without large artifacts even though the image geometry was complex due to the central brightness of the E-Ring. The resulting effect on background is shown in Figure 8.

5.2.4 Provided Image Size Estimators

1. Raw Size at Target
2. Size at Ring Plane

Raw estimate is used by default and simply estimates the image dimensions at target distance. Ring plane size estimator is based on the definition of the IAU SATURN frame (Archinal et al., 2018), where the x,y-plane lies on the axis of rotation. Rings and majority of the satellites orbit near or in this plane (Goldreich and Tremaine, 1982; Harper and Taylor, 1993; M. M. Hedman et al., n.d.). During development this proved to be a useful feature for estimating image sizes on images taken high above the rings and ring targeted images.

The ring intercept estimator displays image size at the IAU Saturn frame x,y-plane, in which the main rings lie and the raw size is the image size at the target distance, both based on the field of view vectors for the instrument from the IK-kernels for the SPICE toolkit. The image size is calculated as a

rectangle formed by these boundary vectors defining the instrument field of view when they are all scaled to extend to the desired distance. For the ring plane size estimator the scaling factor for the boundary vectors is defined by calculating where the boundary vectors intersect the IAU Saturn x,y-plane.

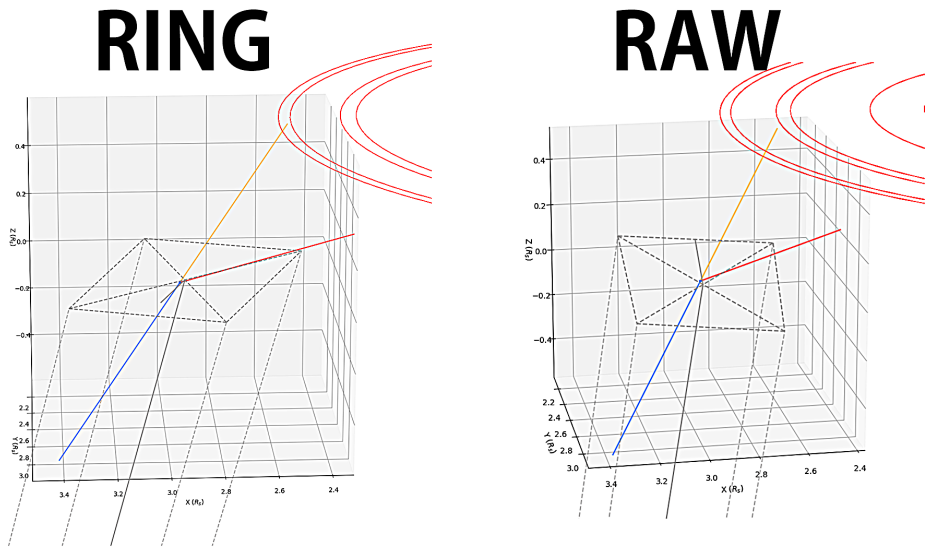

Figure 6: Display of different size estimator geometries and how they are reflected in 3d space. The dashed gray lines mark the boundary vectors for the instrument retrieved from SPICE. The colored lines are the directions of important landmarks. Yellow line marks the direction of the Sun and the Blue line is the continuation of the Yellow line marking the position and direction of the produced shadow. The red line points towards Saturn. The rectangle formed by the dashed gray lines marks the projected image.

5.3 Additional Features

The program also provides additional features, such as extracting image geometry from Cassini kernels using the NAIF SPICE toolkit, which is displayed as image dimensions added to plots and an additional viewer for 3D geometry. The image geometry is recovered with the help of embedded image labels detailed in the VICAR format (Deen, 1992). These labels include identification information of the image including the sequence and image ids and instrument information and telemetry data about the instrument that produced the data product.

The program will use these embedded labels to find out properties contained in the image labels embedded in the label structure as follows:

$$\text{IMAGE} \longrightarrow \text{LABELS} \longrightarrow \textbf{PROPERTY} \longrightarrow \textbf{KEY} \longrightarrow \text{VALUE}$$

The image time:

$$\text{IDENTIFICATION} \longrightarrow \text{IMAGE\_TIME}$$

The exposure time:

$$\text{INSTRUMENT} \longrightarrow \text{EXPOSURE\_DURATION}$$

The image filter list:

$$\text{INSTRUMENT} \longrightarrow \text{FILTER\_NAME}$$

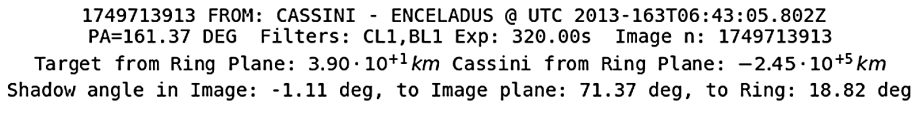

Figure 7: An image title from the program with additional information added. The title contains the image time in UTC, the phase angle of the target in the image given in degrees and extracted from SPICE, image filter list, exposure duration in seconds, offsets from the Saturn ring plane (x,y-plane in IAU Saturn (Archinal et al., 2018)) in kilometers and information about the shadow and its angles. The shadow angles presented are the shadow angle in image, which is the angle between the shadow and the image x-axis, the angle the shadow has with the image plane indicating the amount of foreshortening, how much the shadow protrudes from the image, and the shadow angle with the IAU Saturn ring plane.

5.4 Development and Software Used

The program is freely available at https://github.com/joniumGit/moons.

The program is developed using Python 3 and it consists of two modules *vicarutil* and *vicarui*. The first of the modules provides support for reading the image files and second one provides the visualization and analysis of the images. The name is inspired by the *NASA Vicar* image processing system and the *VICAR* file format that it uses (Deen, 1992). The program is developed with extension in mind, so that it could be extended to analyze images from other missions if the toolkit is found useful for other research projects.

Notable and important libraries used in the development are: Matplotlib (Hunter, 2007), Astropy (Collaboration, 2018, Collaboration, 2013), Scikit (Pedregosa et al., 2011) and Numpy (Harris et al., 2020). All the image geometry data is produced with the NAIF Spice toolkit (C. H. Acton, 1996, C. Acton et al., 2018) and the excellent Python wrapper created for it, Spiceypy(Annex et al., 2020). Statistics for the fitting operations are provided by the models from Statsmodels (Seabold and Perktold, 2010).

6 Analysis and Results

6.1 Data

The data used in this paper is obtained from The PDS Ring-Moon Systems Node's OPUS search service by the Ring-Moon Systems Node at PDS Data System (Gordon et al., 2017). The initial data selection was done by visually inspecting promising images for any shadows present and choosing the images with the clearest shadows. Enceladus had the largest amount of data available and was thus selected for this analysis. The moon Tethys did not have as much data available as Enceladus and the data quality was also not as good, usually placing Tethys at the edges of images or the images were missing lines or had a bad exposure time. The dataset contained some mislabeled data and data with low signal-to-noise ratio, but the reduced dataset was sufficient for this preliminary analysis. All the images used are calibrated versions of the images, using the CISSCAL pipeline version *CISSCAL 4.0beta* as indicated by the accompanying *.LBL* files provided by OPUS. This version of the software includes all important adjustments to the calibration pipeline, excluding the latest polarizer calibrations (Knowles et al., 2020). The tables contain two filters, because the Cassini ISS cameras have two filter wheels for filter selection or combining (Porco et al., 2004). All of the data used here is a combination of a clear filter accompanied by a color filter for a specific wavelength or another clear filter. The wavelengths and names for each filter used are presented in Table 1.

The task of producing meaningful data from the images is difficult. Producing accurate error metrics was difficult during development. After initial failures with error measurements the Statsmodels library was selected to provide reliable Standard Error estimates for the fitted coefficients in the program. This proved to especially useful for the *Autofit*-feature.

The dataset (2) of Enceladus does not include any images from the filters IR2 (852 nm) and IR1 (740 nm) as all the images collected failed to display any measurable shadow or the shadow resolution was too small to be used. Datasets (4) and (5) do not include anything with wavelengths longer than the IR1 filter as all the images failed to show measurable shadows for Tethys. Wavelengths and filter information is gathered from Porco et al., 2004.

The following part shows processes used during the shadow analysis and lists the datasets used.

6.2 Methods

Images were first manually selected to be included in the datasets by inspecting them for visible shadows. A single round of *Autofit* was run for each image and the shadow contrast plot (Fig. 9), was inspected to ensure that the image was able to be analyzed by the tool. These initial steps helped narrow down the data from several tens of images to only a few promising images per filter for each target. After the initial round of rejections the final dataset was then manually inspected again and the most promising images were selected for analysis.

For Tethys the analysis consisted of inspecting the shadow using the *Autofit* procedure without fitting any functional forms to produce plots that display the shadow contrast as a function of distance. For Enceladus a similar approach was selected, but instead of displaying shadow plots, an approach was selected to inspect the "near" area seen in Fig. 8, which is the bright inner area near Enceladus, and try to see if there is any noticeable differences in different filters.

Filter	λ_{eff}	Description
CL1	634	Wide open, clear filter
CL2	634	Wide open, clear filter
BL1	463	Blue, color
GRN	568	Green, color
RED	647	Red, color
IR1	740	Infrared, color
IR3	917	Infrared, color

Table 1: The filters in Cassini ISS as described in Porco et al., 2004. The wavelength used is the effective wavelegth given in the table in Porco et al., 2004 p. 84

DATASET 1: ENCELADUS 1 PHASE ANGLE 163 ± 3 DEG

Image ID	Filters		Exposure(s)
1749713913	CL1	BL1	320
1749716690			320
1749711485	CL1	CL2	22
1749714685			22
1749715000			22
1749717540			22
1749716028	CL1	RED	46
1749713251			46
1749715662	IR3	CL2	320

Table 2: Dataset 1 consisting of Enceladus targeted images with multiple filters.

DATASET 2: ENCELADUS 2 PHASE ANGLE 162 ± 3 DEG

Image ID	Filters		Exposure(s)
1853519736	CL1	CL2	38
1853519911			68
1853523096			38

Table 3: Dataset 2 consists of additional Enceladus images, but with a significantly different geometry compared to Dataset 1 in table 2.

DATASET 3: TETHYS 1	173 ± 1 DEG		
Image ID	Filters		Exposure(s)
1537013345	CL1	BL1	10
1537014673			10
1537013313	CL1	GRN	2
1537014641			2
1537013154	CL1	CL2	1
1537013194			4.6
1537013296	CL1	RED	2
1537014624			2
1537013395	CL1	IR1	2
1537014731			2

Table 4: Dataset 3 consists of Tethys images only. Contains mostly very hard to analyze geometry with Tethys right at the image edge.

DATASET 4: TETHYS 2	168 ± 1 DEG		
Image ID	Filters		Exposure(s)
1870759110	CL1	BL1	38
1870759142	CL1	GRN	6.80
1870759174	CL1	RED	46

Table 5: Dataset 4 consists of images of Tethys only

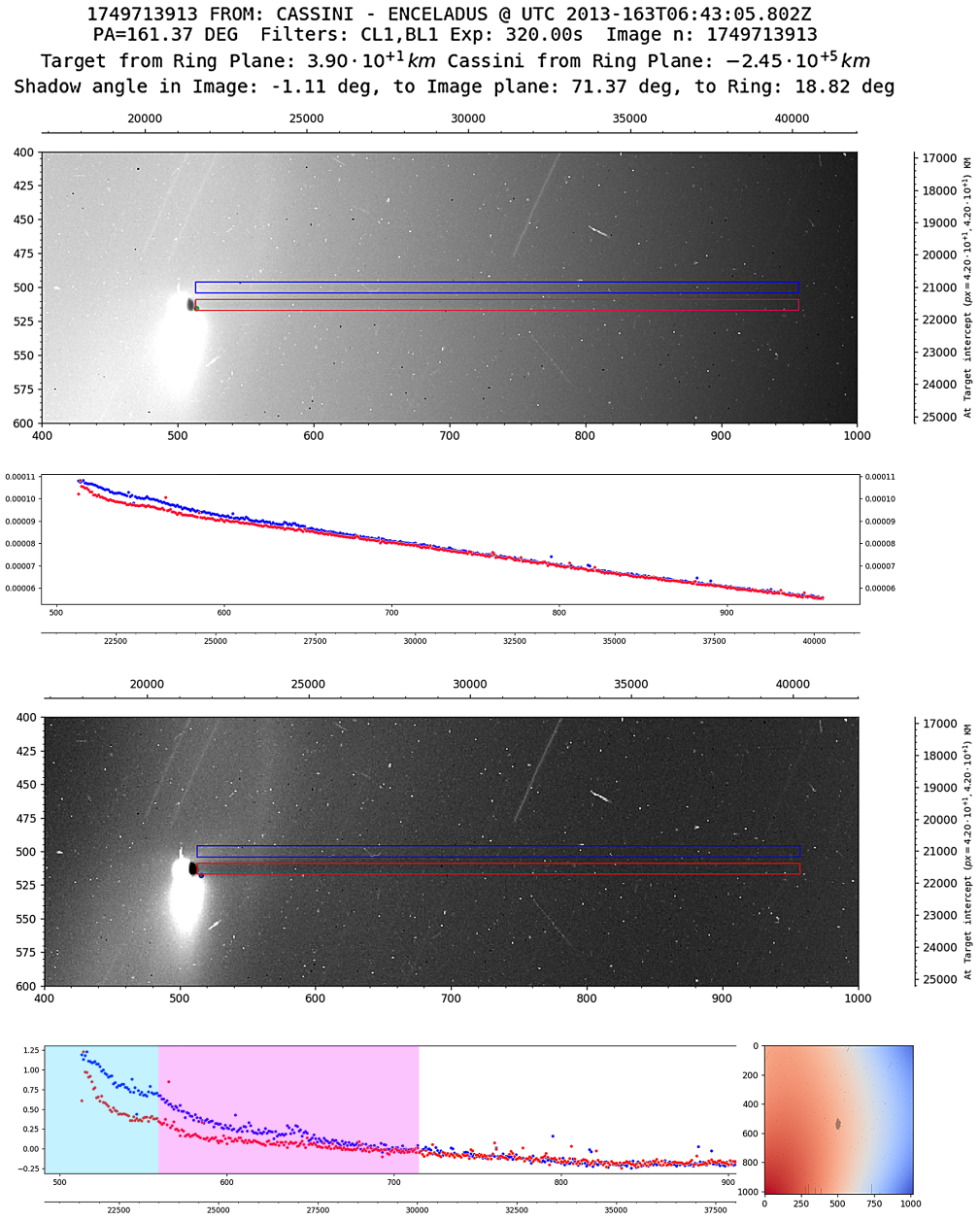

Figure 8: W1749713913 - Image with almost horizontal shadow relative to the image x-axis allows the comparison of shadow features easily. The plots show the difference between background and shadow with (Lower Panel) and without (Upper Panel) background subtraction applied. Two different shadow regions can be identified from the lower panel where the shadow contrast behaves differently indicating a change in the local ring properties. In the magenta region the shadow contrast decreases along with the distance, but the cyan region show the contrast staying near constant after initial drop-off near the beginning. The cyan region roughly corresponds to the central bright region around Enceladus' orbit visible in Fig. 1. Explanation on the metrics in the image title is presented in Fig. 7.

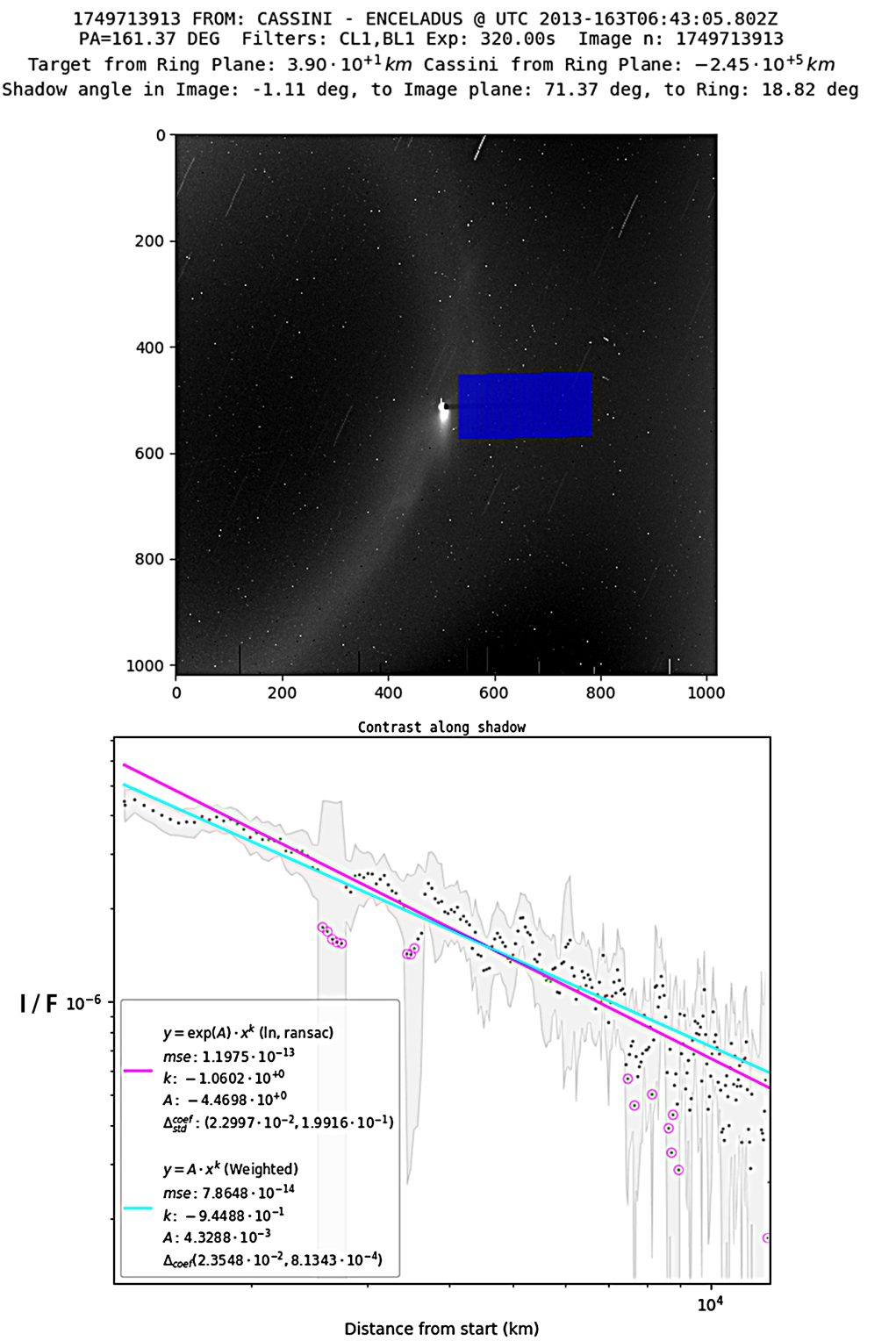

Figure 9: A plot from the analysis tool *Autofit* trying to fit two lines describing a power law to the extracted shadow data. The magenta line represents a log-linearized powerlaw and the Cyan line is a direct error accounting fit for a power law. It can be seen that both fits are "bad" and that the shadow contrast profile itself does not appear completely linear on a log-log scale showing that the fit is ill-advised.

6.3 Results

6.3.1 Enceladus

Some investigation was done to possible functional forms that might fit the shadow data. In Fig. 9, the shadow contrast for the inner region near Encelauds' orbit is plotted on a log-log scale and a power law is fitted to it. Trying a power law was based on the functional forms used in Tamayo et al., 2014. No *a-priori* assumption of a power law can be done as there is no need or direct reason for the shadow contrast fall-off to obey a power law. The relation is purely empirical through trying different forms that might fit. The shadow contrast is connected with the local ring properties and most likely cannot be described by a single functional form as seen in Fig. 8 and 9. Fig. 9 shows that a single fit wouldn't explain the shadow contrast, which would make sense even from a visual inspection of the image as it shows ring particle density variation as increased brightness near the orbit of Enceladus corresponding to a higher particle density in that area, see Fig. 1, 8. The profiles presented here could serve as the basis for further research as they already show that the visually seen variations of the ring can be seen in the shadow data.

Perhaps it would be possible to connect measurements from multiple images where the shadow changes place to use methods already proven valid in Tamayo et al., 2014 or use the stacking method described there. A short experiment on stacking images was performed to see if a conical shadow could be produced as a result as described in Tamayo et al., 2016, presented in Fig. 10, but the results were inconclusive. However, Fig. 10 does show that even a simple stacking method can produce a noticeable improvement on the image quality when assessing it in terms of visibility of the shadow. For the stacking experiment 11x26s exposures sharing similar geometry were collected and stacked by averaging them. The result showed a smooth background with the dimmest stars removed completely, but produced artifacts from overexposed pixels as seen in Fig. 10. These artifacts could certainly be removed to produce a very smooth image containing nearly no stars or artifacts, with only the E-Ring data remaining. An easy solution for an improved solution would to take the iterative staking method from Tamayo et al., 2014 where pixels are rejected if they are a certain number of standard deviations from the mean, which should remove the stars.

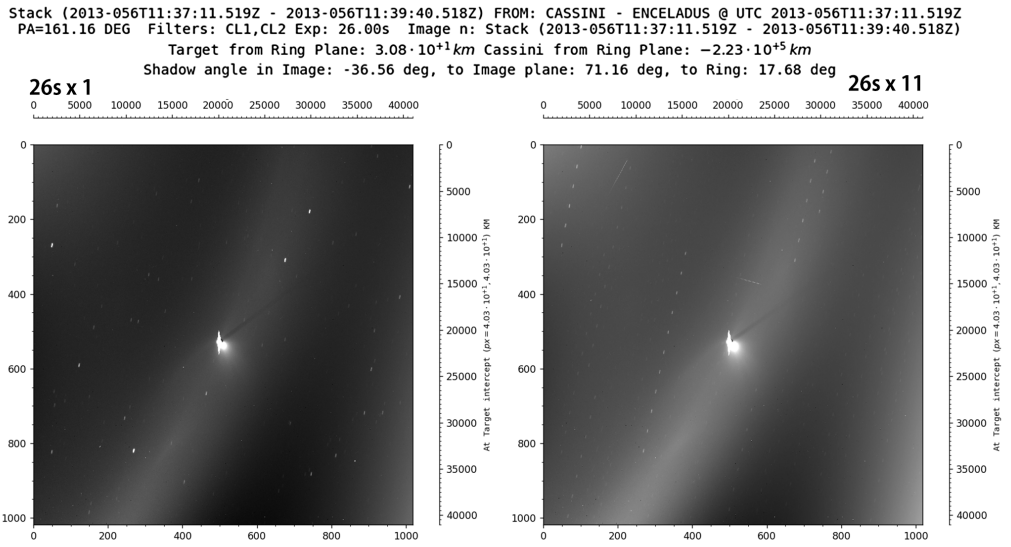

Figure 10: The result of stacking (Right Panel) versus a single frame (Left Panel). An experiment was carried out to see if a stack could be produced where the shadow changes position slightly in every frame to produce a slightly conical shadow covering more area in the image, for which the result was inconclusive. The end result was a success nevertheless as the stacking removed most of the dim background artifacts and reduced noise, while still maintaining the shadow shape, which was unexpected, due to the very good alignment between the images. Due to the stack being a simple average of the images, the brightest artifacts still remain as their effect was too large even for a 11 image average. The time interval for the image stack is shown at the top along with other image information detailed earlier in Fig. 7. The information is fetched from the master image of the stack, which was defined to be the first image in this case.
Images used (Calibrated): **W1740486700**, W1740486849, W1740486998, W1740487147, W1740487296, W1740487445, W1740487594, W1740487743, W1740487892, W1740488041, W1740488190.

FILTER	K	ΔK	A	ΔA
BL1	$-7.79 \cdot 10^{-1}$	$4.33 \cdot 10^{-2}$	$1.67 \cdot 10^{-2}$	$5.32 \cdot 10^{-4}$
CL2	$-8.39 \cdot 10^{-1}$	$7.61 \cdot 10^{-2}$	$2.84 \cdot 10^{-3}$	$2.06 \cdot 10^{-3}$
RED	$-8.95 \cdot 10^{-1}$	$5.94 \cdot 10^{-2}$	$4.73 \cdot 10^{-3}$	$2.52 \cdot 10^{-3}$
IR3	$-8.17 \cdot 10^{-1}$	$8.78 \cdot 10^{-2}$	$1.82 \cdot 10^{-3}$	$1.23 \cdot 10^{-3}$
CL2	$-1.18 \cdot 10^{0}$	$2.30 \cdot 10^{-1}$	$1.04 \cdot 10^{-1}$	$2.09 \cdot 10^{-1}$

Table 6: Datasets 2 (Top) and 3 (Bottom) fitted parameters after attempting to fit a power law to the central ring region shadow.

Having fitted the power law ($y = Ax^K$) to the available Enceladus data as can be seen in table 6 we can conclude that the results seem comparable for similar geometry, but show a significant difference in different geometry. This means that images from one sequence could be compared together, but making a comparison with another image sequence might be difficult. From the top part of the table we can see slight variations in the coefficients, most of which are within error margins of the other coefficients, but the A coefficient showing a very high error. Due to the data showing significant difference between different geometries, even though the inspected area did not change and one of the parameters shows great variance, leads to the conclusion that something has gone wrong during the fitting procedure. It could be that the fits were badly placed or bad parameters used, but a more reasonable explanations is the fact that the power law fit was achieved through empirical testing on a limited number of images, so seeing it perform badly here is not too surprising as it is needed to recall the earlier note that there should be no assumption for a power law due to the shadow properties being connected to the local ring properties which can vary in multiple ways and do not necessary show characteristics of any simple functional form as there are many things to take into account from proximity to Enceladus, to the local plasma environment (Horányi et al., 2009; Kempf et al., 2010; Srama et al., 2011).

The differences between the blue filter and the rest for both coefficients is still significant and warrants more investigation. However, looking at Fig. 11 we can see that the shadow contrast profiles for both the red and blue filters are quite alike, so it should be unlikely to find major differences in coefficients when fitting to the data considering that their separation is on the scale of $\cdot 10^{-7}$, which again points to a possible fault on the plotting analysis presented in Table 6.

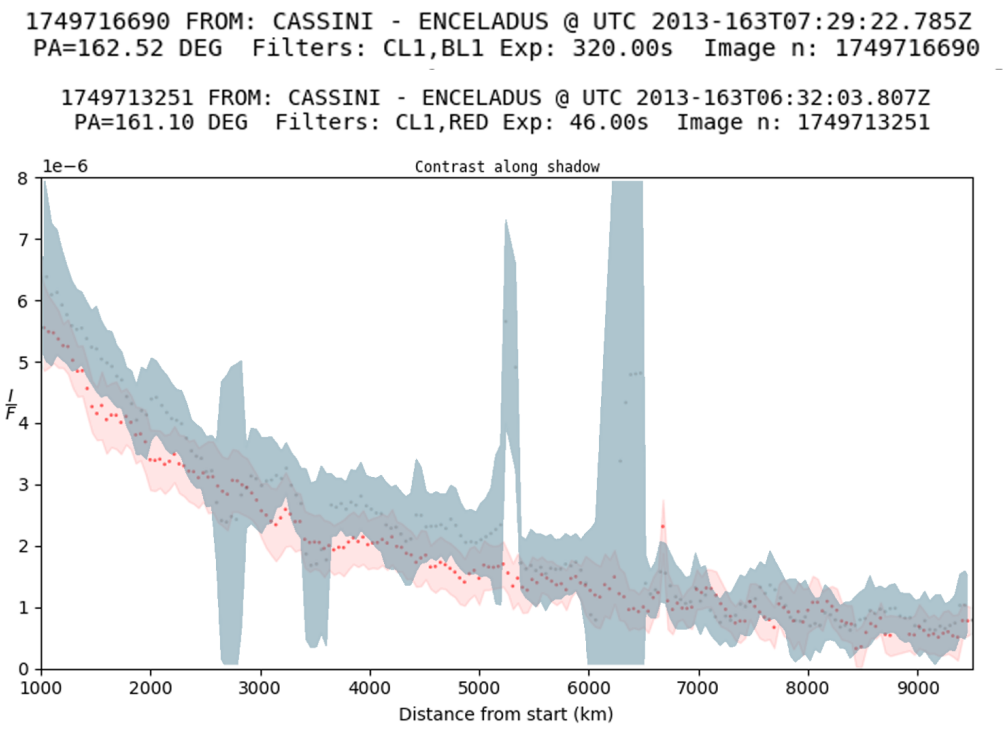

Figure 11: Comparison of two image shadow contrasts in filters RED and BL1. The shadows show a very similar profile for the whole distance along the shadow. The blue plot has larger error, but the shapes of the plot are nearly identical. It should be noted that since the plot shows the value of the shadow contrast, that the blue plot is consistently higher than the red one indicating that the blue image has a larger shadow contrast, perhaps due to the slightly higher phase angle. In the figure the x-label start is referring to the target of the image, in this case Enceladus.

6.3.2 Tethys

Following are the shadow contrast profiles produced for Tethys:

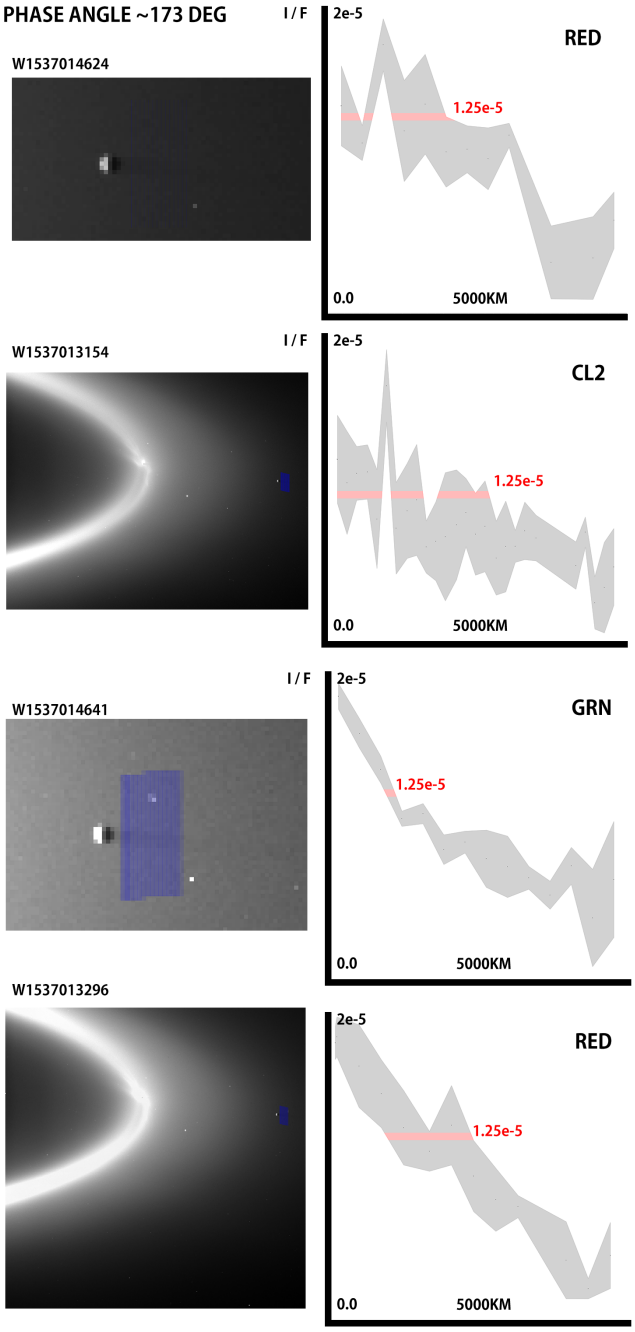

Figure 12: Overview of extracted shadow contrast profiles for dataset 4 showing the difficulty of extracting reliable data from a low resolution images. The error margins are fairly large. The red line is marked to provide a comparison point for shadow features and their relative locations, but has no physical significance in the data.

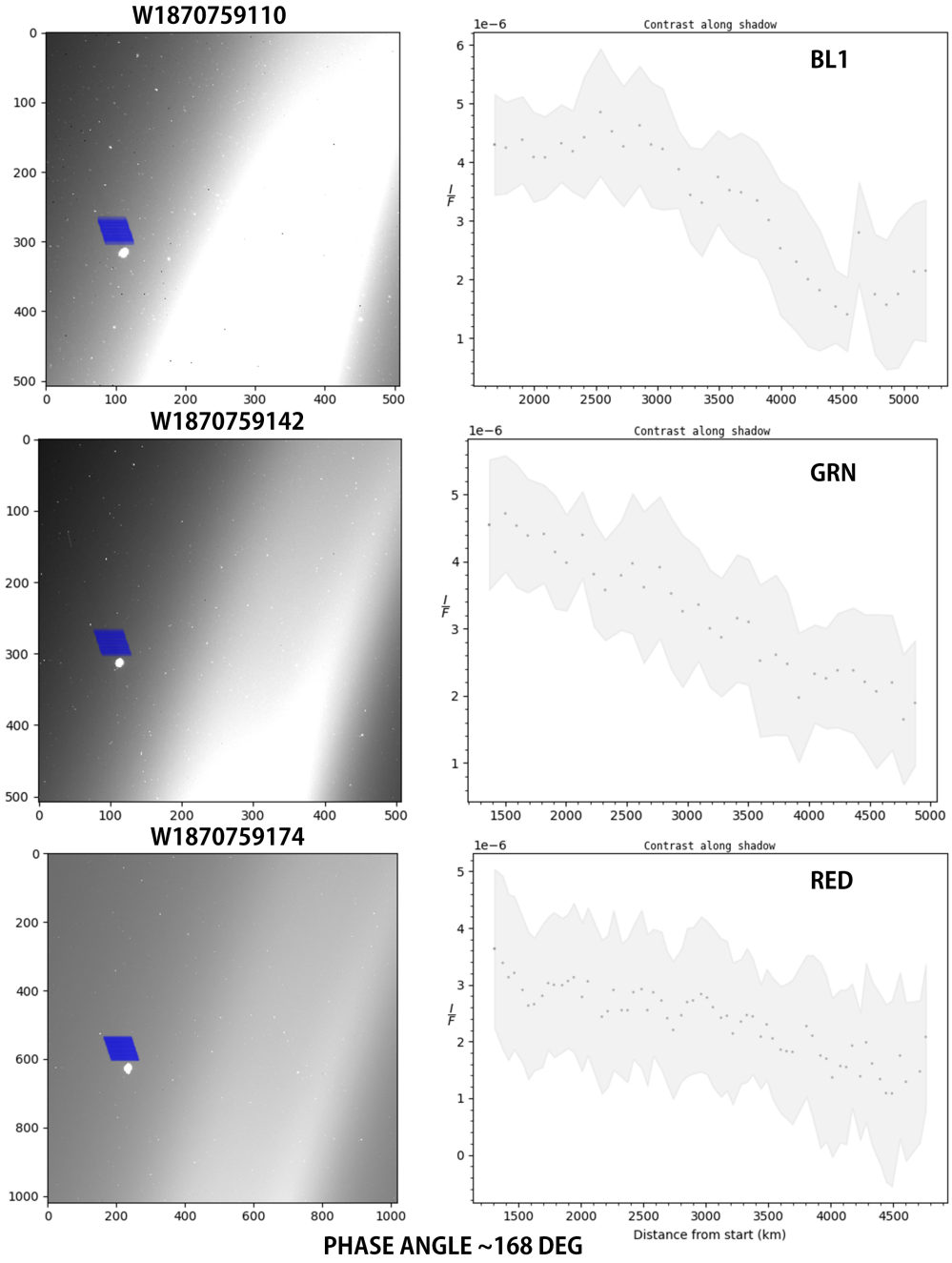

Figure 13: Extracted shadow profiles from dataset 3. The blue areas in the left images represent the sampling area shown in the right side plots. The black dots are measurement points and the gray area is the error margin. The shadow plots show similar features as seen in Fig. 12

For Tethys the analysis is a success. The produced shadow contrast plots are able to show that there exists noticeable differences between different filters. Looking at Fig. 12 and 13 we an see an interesting effect for both datasets, the green and red filter consistently produce shadow profiles with less error than any other filter and the shadow continues to be detectable to a longer distance from the target. At this stage it is too early to say why this happens, but it definitely warrants more investigation.

From Fig. 12 we can see that even the images where Tethys is right at the edge can produce a shadow contrast profile. For further research Tethys should be an area of interest as the local ring environment at the distance of its orbit should be more regular than at Enceladus, where significant differences in the ring can be seen even on visual inspection (M. Hedman et al., 2012; Ingersoll and Ewald, 2011; Ye et al., 2016). Here the previously much discussed image processing methods from Tamayo et al., 2014 should be very helpful for extracting more information about the shadows.

When looking at the figures 12 and 13 it is clear that the red and green filters have produced a profile with much less error than the other filters. This should warrant more research on the differences seen between different filters, if the difference is visible at Tethys distance, then it certainly should be observable at Enceladus too.

7 Conclusions and Further Research

7.1 Shadow Contrast

The preliminary analysis showed that it is feasible to extract shadow contrast from images and that it can be done in a reproducible way. The main goals outlined for this paper were reached. The methods viability for further research was demonstrated and that there is sufficient data available for a in-depth analysis. On the assumption that the remaining problems with the program, data and analysis methods can be solved, it is clear that the topic has need for further analysis.

7.2 Considerations for Further Research

The available image data with easily analyzable shadows was sufficient for this preliminary analysis. The main challenges working with the data were the difficulties of working with noisy, low resolution and limited data analysis tools. A more diverse dataset is needed if a more comprehensive analysis is

to be performed. There is a lot of image data available on Enceladus and with further analysis it can be used to constrain the shadow properties even better and with higher accuracy in the future.

Except for Enceladus, the data on the other outer moons is limited. The second most diverse dataset was of Tethys, but mostly low resolution data. An analysis on the data quality and quantity for other outer moons needs to be performed if the shadow properties are to be mapped on a larger area. Any further researcher should expect and prepare to work with limited data, limited in quality and quantity and variety. Also, it cannot be assured that usable data is available for all filter combinations.

For further research on the topic, a more varied data set should be collected. The dataset used here is limited and lacks variety in the filters used. Further considerations should also include a way to stack or denoise low signal-to-noise ratio images, so that they could be used for analysis, especially NAC images are of interest here. A problem with some images is that the shadow is visible on visual inspection, but gets lost in the noise when trying to produce a shadow contrast graph for it, but this could be alleviated with the previously mentioned denoising methods.

Any further research should find ways to combine these results to existing research (Ingersoll and Ewald, 2011; Kempf et al., 2010; Porco, 2006).

7.3 Acknowledgements

The guidance and feedback from J. Schmidt was invaluable for this paper. I'm grateful for Z. Peng for helpful discussion on machine learning models. I acknowledge the Spiceypy and SKlearn libraries for their helpful and informative learning materials which helped immensely in the development of the analysis tools used in this paper. I am grateful for the efforts of the NAIF SPICE toolkit development team that made all image geometry analysis possible.

References

Acton, C., Bachman, N., Semenov, B., & Wright, E. (2018). A look towards the future in the handling of space science mission geometry. *Planetary and Space Science*, *150*, 9–12. https://doi.org/10.1016/j.pss.2017.02.013

Acton, C. H. (1996). Ancillary data services of NASA's navigation and ancillary information facility. *Planetary and Space Science*, *44*(1), 65–70. https://doi.org/10.1016/0032-0633(95)00107-7

Annex, A., Pearson, B., Seignovert, B., Carcich, B., Eichhorn, H., Mapel, J., von Forstner, J., McAuliffe, J., del Rio, J., Berry, K., Aye, K.-M., Stefko, M., de Val-Borro, M., Kulumani, S., & Murakami, S.-y. (2020). SpiceyPy: A pythonic wrapper for the SPICE toolkit. *Journal of Open Source Software*, *5*(46), 2050. https://doi.org/10.21105/joss.02050

Archinal, B. A., Acton, C. H., A'Hearn, M. F., Conrad, A., Consolmagno, G. J., Duxbury, T., Hestroffer, D., Hilton, J. L., Kirk, R. L., Klioner, S. A., McCarthy, D., Meech, K., Oberst, J., Ping, J., Seidelmann, P. K., Tholen, D. J., Thomas, P. C., & Williams, I. P. (2018). Report of the IAU working group on cartographic coordinates and rotational elements: 2015. *Celestial Mechanics and Dynamical Astronomy*, *130*(3). https://doi.org/10.1007/s10569-017-9805-5

Choi, S., Kim, T., & Yu, W. (2009). Performance evaluation of RANSAC family. *Procedings of the British Machine Vision Conference 2009*. https://doi.org/10.5244/c.23.81

Collaboration, T. A. (2013). *Astronomy & Astrophysics*, *558*, A33. https://doi.org/10.1051/0004-6361/201322068

Collaboration, T. A. (2018). The astropy project: Building an open-science project and status of the v2.0 core package. *The Astronomical Journal*, *156*(3), 123. https://doi.org/10.3847/1538-3881/aabc4f

Cuzzi, J. N., Burns, J. A., Charnoz, S., Clark, R. N., Colwell, J. E., Dones, L., Esposito, L. W., Filacchione, G., French, R. G., Hedman, M. M., Kempf, S., Marouf, E. A., Murray, C. D., Nicholson, P. D., Porco, C. C., Schmidt, J., Showalter, M. R., Spilker, L. J., Spitale, J. N., ... Weiss, J. (2010). An Evolving View of Saturn's Dynamic Rings. *Science*, *327*(5972), 1470–1475. https://doi.org/10.1126/science.1179118

Deen, R. G. (1992). *VICAR file format documentation*. Retrieved May 8, 2021, from https://www-mipl.jpl.nasa.gov/external/VICAR_file_fmt.pdf

Derpanis, K. (2005). Overview of the ransac algorithm.

Goldreich, P., & Tremaine, S. (1982). The dynamics of planetary rings. *Annual Review of Astronomy and Astrophysics*, *20*(1), 249–283. https://doi.org/10.1146/annurev.aa.20.090182.001341

Gordon, M. K., Showalter, M. R., Ballard, L., Tiscareno, M., French, R. S., & Olson, D. (2017). OPUS: A Comprehensive Search Tool for Remote Sensing Observations of the Outer Planets. Now with Enhanced Geometric Metadata for Cassini and New Horizons Optical Remote

Sensing Instruments. *Third Planetary Data Workshop and The Planetary Geologic Mappers Annual Meeting*, *1986*, Article 7088, 7088.

Graff, P., Feroz, F., Hobson, M. P., & Lasenby, A. (2014). SkyNet: An efficient and robust neural network training tool for machine learning in astronomy. *Monthly Notices of the Royal Astronomical Society*, *441*(2), 1741–1759. https://doi.org/10.1093/mnras/stu642

Gwyn, S. D. J. (2008). MegaPipe: The MegaCam image stacking pipeline at the canadian astronomical data centre. *Publications of the Astronomical Society of the Pacific*, *120*(864), 212–223. https://doi.org/10.1086/526794

Harper, D., & Taylor, D. B. (1993). The orbits of the major satellites of Saturn. *Astronomy and Astrophysics*, *268*, 326–349.

Harris, C. R., Millman, K. J., van der Walt, S. J., Gommers, R., Virtanen, P., Cournapeau, D., Wieser, E., Taylor, J., Berg, S., Smith, N. J., Kern, R., Picus, M., Hoyer, S., van Kerkwijk, M. H., Brett, M., Haldane, A., del Río, J. F., Wiebe, M., Peterson, P., ... Oliphant, T. E. (2020). Array programming with NumPy. *Nature*, *585*(7825), 357–362. https://doi.org/10.1038/s41586-020-2649-2

Hedman, M. M., Postberg, F., Hamilton, D. P., Renner, S., & Hsu, H.-W. (n.d.). Dusty rings. *Planetary ring systems* (pp. 308–337). Cambridge University Press. https://doi.org/10.1017/9781316286791.012

Hedman, M., Burns, J., Hamilton, D., & Showalter, M. (2012). The three-dimensional structure of saturn's e ring. *Icarus*, *217*(1), 322–338. https://doi.org/10.1016/j.icarus.2011.11.006

Horányi, M., Burns, J. A., Hedman, M. M., Jones, G. H., & Kempf, S. (2009). Diffuse rings. *Saturn from cassini-huygens* (pp. 511–536). Springer Netherlands. https://doi.org/10.1007/978-1-4020-9217-6_16

Hunter, J. D. (2007). Matplotlib: A 2d graphics environment. *Computing in Science & Engineering*, *9*(3), 90–95. https://doi.org/10.1109/MCSE.2007.55

Ingersoll, A. P., & Ewald, S. P. (2011). Total particulate mass in enceladus plumes and mass of saturn's e ring inferred from cassini ISS images. *Icarus*, *216*(2), 492–506. https://doi.org/10.1016/j.icarus.2011.09.018

Kempf, S., Beckmann, U., & Schmidt, J. (2010). How the Enceladus dust plume feeds Saturn's E ring. *Icarus*, *206*(2), 446–457. https://doi.org/10.1016/j.icarus.2009.09.016

Knowles, B., West, R., Helfenstein, P., Verbiscer, A., Wilson, D., & Porco, C. (2020). End-of-mission calibration of the cassini imaging science subsystem. *Planetary and Space Science*, *185*, 104898. https://doi.org/10.1016/j.pss.2020.104898

Pedregosa, F., Varoquaux, G., Gramfort, A., Michel, V., Thirion, B., Grisel, O., Blondel, M., Prettenhofer, P., Weiss, R., Dubourg, V., Vanderplas, J., Passos, A., Cournapeau, D., Brucher, M., Perrot, M., & Duchesnay, E. (2011). Scikit-learn: Machine learning in Python. *Journal of Machine Learning Research*, *12*, 2825–2830.

Porco, C. C. (2006). Cassini Observes the Active South Pole of Enceladus. *Science*, *311*(5766), 1393–1401. https://doi.org/10.1126/science.1123013

Porco, C. C., West, R. A., Squyres, S., Mcewen, A., Thomas, P., Murray, C. D., Delgenio, A., Ingersoll, A. P., Johnson, T. V., Neukum, G., Veverka, J., Dones, L., Brahic, A., Burns, J. A., Haemmerle, V., Knowles, B., Dawson, D., Roatsch, T., Beurle, K., & Owen, W. (2004). Cassini imaging science: Instrument characteristics and anticipated scientific investigations at saturn. *Space Science Reviews*, *115*(1-4), 363–497. https://doi.org/10.1007/s11214-004-1456-7

Puetter, R., Gosnell, T., & Yahil, A. (2005). Digital image reconstruction: Deblurring and denoising. *Annual Review of Astronomy and Astrophysics*, *43*(1), 139–194. https://doi.org/10.1146/annurev.astro.43.112904.104850

Schmidt, J., Brilliantov, N., Spahn, F., & Kempf, S. (2008). Slow dust in enceladus' plume from condensation and wall collisions in tiger stripe fractures. *Nature*, *451*(7179), 685–688. https://doi.org/10.1038/nature06491

Seabold, S., & Perktold, J. (2010). Statsmodels: Econometric and statistical modeling with python. *9th Python in Science Conference*.

Spilker, L. (2019). Cassini-huygens' exploration of the saturn system: 13 years of discovery. *Science*, *364*(6445), 1046–1051. https://doi.org/10.1126/science.aat3760

Srama, R., Kempf, S., Moragas-Klostermeyer, G., Altobelli, N., Auer, S., Beckmann, U., Bugiel, S., Burton, M., Economomou, T., Fechtig, H., Fiege, K., Green, S. F., Grande, M., Havnes, O., Hillier, J. K., Helfert, S., Horanyi, M., Hsu, S., Igenbergs, E., ... Röser, H.-P. (2011). The cosmic dust analyser onboard cassini: Ten years of discoveries. *CEAS Space Journal*, *2*(1-4), 3–16. https://doi.org/10.1007/s12567-011-0014-x

Tamayo, D., Hedman, M. M., & Burns, J. A. (2014). First observations of the phoebe ring in optical light. *Icarus*, *233*, 1–8. https://doi.org/10.1016/j.icarus.2014.01.021

Tamayo, D., Markham, S. R., Hedman, M. M., Burns, J. A., & Hamilton, D. P. (2016). Radial profiles of the phoebe ring: A vast debris disk

around saturn. *Icarus*, *275*, 117–131. https://doi.org/10.1016/j.icarus.2016.04.009

Verbiscer, A. J., Skrutskie, M. F., & Hamilton, D. P. (2009). Saturn's largest ring. *Nature*, *461*(7267), 1098–1100. https://doi.org/10.1038/nature08515

Virtanen, P., Gommers, R., Oliphant, T. E., Haberland, M., Reddy, T., Cournapeau, D., Burovski, E., Peterson, P., Weckesser, W., Bright, J., van der Walt, S. J., Brett, M., Wilson, J., Millman, K. J., Mayorov, N., Nelson, A. R. J., Jones, E., Kern, R., Larson, E., ... SciPy 1.0 Contributors. (2020). SciPy 1.0: Fundamental Algorithms for Scientific Computing in Python. *Nature Methods*, *17*, 261–272. https://doi.org/10.1038/s41592-019-0686-2

Ye, S.-Y., Gurnett, D., & Kurth, W. (2016). In-situ measurements of saturn's dusty rings based on dust impact signals detected by cassini RPWS. *Icarus*, *279*, 51–61. https://doi.org/10.1016/j.icarus.2016.05.006